Compact cylindrical multipass cell for laser absorption spectroscopy

Chao Shen (沈 超)*, Yujun Zhang (张玉钧), and Jiazheng Ni (倪家正)

State Key Laboratory of Pulsed Power Laser Technology, Electronic Engineering Institute, Hefei 230037, China

**Corresponding author: zhouxue19891020@sina.com*

Received March 8, 2013; accepted May 13, 2013; posted online August 9, 2013

A compact multipass cell with low fringes and high thermal stability is described. This cell is formed by two twisted cylindrical mirrors. The optical parameters are determined based on the selection criteria, which include mirror filling efficiency, interference fringes, and pattern stability. With a pattern of 174 passes, this cell gives a 22-m path length in a volume of 0.55 L. The results of an absorption measurement of oxygen at 13 091.7 cm^{-1} show that the fringe noise is lower than 6.54×10^{-4}. The maximum allowed temperature change to keep the beam from exiting is 33 K, which indicates high stability against thermal drift.

OCIS codes: 120.1880, 120.4640, 120.4880.
doi: 10.3788/COL201311.091201.

Multipass cells are widely used in laser absorption spectroscopy because these devices can provide long path lengths in a relatively small volume[1,2]. After several decades of cell design developments, the most promising cell to date is the laser resonator, which is based on two twisted cylindrical mirrors[3−6]. This cylindrical cell has the advantages of high spot density, easy alignment, and low cost, and has been utilized with different configurations for specific purposes[7,8]. However, most of the design considerations for this cell only focus on the pass numbers; no further criteria for pattern choosing are revealed. In fact, considerations of the mirror filling efficiency, interference fringes, and stability of the different patterns are vital to cell design particularly when a high pass number is used. In this letter, we propose a relatively complete design consideration of a cylindrical cell and then describe a compact cell design based on these conclusions. Finally, an absorption measurement for determining the cell's usefulness is performed.

The basic geometry of the multipass cell is shown in Fig. 1. The coordinate system in the figure is the Cartesian coordinate system. The center of the front cylindrical mirror M_1 is located at $z = 0$, whereas the back mirror M_2 is at $z = d$. The focal lengths of M_1 and M_2 are f_1 and f_2, respectively. Both mirrors are initially aligned with the x axis and are then twisted by angles of τ_1 and τ_2, respectively. M_1 has a central hole whose center coincides with the origin of the coordinate system. The input and output beams through the hole are shown as solid and dashed lines, respectively, in Fig. 1. Beam spot positions are indicated as (x_i, y_i). Reflection spots on M_1 are marked as 0, 2, $4\cdots2N$, whereas the spots on M_2 are labeled as 1, 3, $5\cdots2N$–1, where N is the round-trip number. To determine the accurate beam spot coordinates, the ray can be expressed as a state vector, $\mathbf{Z}_N = [x_{2N+1}, x_{2N}, y_{2N+1}, y_{2N}]^{\mathrm{T}}$, where T denotes transposition. A typical configuration consists of two identical mirrors $f_1 = f_2 = f$ and a symmetric twist angle $\tau_1 = -\tau_2 = \pm\tau$.

According to the derivation in Ref. [9], the analytical expression of $\mathbf{Z}_N$ can be written as

$$\mathbf{Z}_N = \begin{Bmatrix} (x_1 - \Psi y_1)\, C_{\mathrm{U}} \sin\left[(N+1/2)\,\theta_{\mathrm{U}}\right] + \Psi\,(y_1 - \Psi x_1)\, C_{\mathrm{L}} \sin\left[(N+1/2)\,\theta_{\mathrm{L}}\right] \\ (x_1 - \Psi y_1)\, C_{\mathrm{U}} \sin\left(N\theta_{\mathrm{U}}\right) - \Psi\,(y_1 - \Psi x_1)\, C_{\mathrm{L}} \sin\left(N\theta_{\mathrm{L}}\right) \\ (y_1 - \Psi x_1)\, C_{\mathrm{L}} \sin\left[(N+1/2)\,\theta_{\mathrm{L}}\right] + \Psi\,(x_1 - \Psi y_1)\, C_{\mathrm{U}} \sin\left[(N+1/2)\,\theta_{\mathrm{U}}\right] \\ (y_1 - \Psi x_1)\, C_{\mathrm{L}} \sin\left(N\theta_{\mathrm{L}}\right) - \Psi\,(x_1 - \Psi y_1)\, C_{\mathrm{U}} \sin\left(N\theta_{\mathrm{U}}\right) \end{Bmatrix} \left(1 - \Psi^2\right)^{-1}, \tag{1}$$

where $\Psi = [\sum \sqrt{\sum^2 - y\varepsilon^2}]/(2\varepsilon)$, $\sum = \psi - dg$, $\varepsilon = -\sin(\tau)\cos(\tau)dg$, $g = 1/f$, $C_{\mathrm{U,L}} = \sin^{-1}(\theta_{\mathrm{U,L}}/2)$, $\cos\theta_{\mathrm{U,L}} = (\beta^2_{\mathrm{U,L}} + \Psi\beta^2_{\mathrm{L,U}})/[2(1+\Psi^2)] - \varepsilon^2/2 - 1$, $B_{\mathrm{U}} = 2 - dg\cos^2(\tau)$, $\beta_{\mathrm{L}} = 2 - dg\sin^2(\tau)$.

Therefore, the beam spot pattern is determined by θ_{U} and θ_{L}, i.e., the ratios of the distance to the focal length dg and to the rotation angle τ, respectively. Meanwhile, the position of the first spot (x_1, y_1) or the direction of the injecting beam acts as a scale factor that affects the relative distance between the beam spots. The ratio dg, rather than the absolute focal length $1/g$, determines the spot pattern, indicating that the

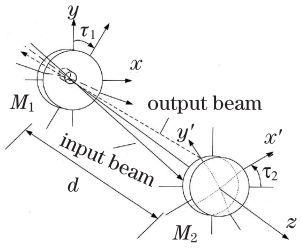

Fig. 1. Basic geometry of a cylindrical multipass cell.

manufacturing imprecision of the mirror can be accommodated by adjustments in mirror separation.

To perform a re-entrant pattern, i.e., $(x_{2N}, y_{2N}) = (0,0)$, $\sin(N\theta_{\rm U})$ and $\sin(N\theta_{\rm L})$ should simultaneously equal 0, which yields

$$\theta_{\rm U} = M_{\rm U}\pi/N, \theta_{\rm L} = M_{\rm L}\pi/N, \tag{2}$$

where $M_{\rm U}$ and $M_{\rm L}$ are both integers. Given a set of $M_{\rm U}$ and $M_{\rm L}$, one can determine the necessary ratio dg and rotation angle τ and achieve the desired number of passes. Notably $M_{\rm U}$ and $M_{\rm L}$ have a period of $2N$ because of the 2π period of the cosine function. The key element in cylindrical multipass cell designs is in choosing a suitable $M_{\rm U}$ and $M_{\rm L}$ pair. From a practical perspective, the output beam should be separated from the input beam to provide sufficient room for the detector and the laser diode. One simple solution is to make both $M_{\rm U}$ and $M_{\rm L}$ even, yielding $\sin[(N-1/2)\theta_{\rm U,L}] = -\sin(\theta_{\rm U,L}/2) = -C_{\rm U,L}$ and $(x_{2N-1}, y_{2N-1}) = -(x_1, y_1)$ according to Eq. (1). In this case, the laser beam exits the cell at an inverted angle, thus simplifying the optical alignment. In addition, $\sin(N\theta_{\rm U,L}/2)$ is also zero, indicating that the Nth spot always lies at the center of the mirror. With an even N, the Nth spot will lie on the front mirror and cause an early exit from the cell before completing the circulation. Thus, an extra constraint condition ensures that N is odd. More extensive considerations involving the examination of different patterns in terms of the mirror filling efficiency, interference fringes, and pattern stability are discussed in the subsequent paragraphs.

The mirror filling efficiency is determined by the relative sizes of the pattern filling area and the mirror area. A typical pattern shape is the parallelogram. From Eq. (1), the parallelogram boundary is limited to a rectangle, whose extreme point is at

$$\begin{cases} x_{\max} = [|(x_1 - \Psi y_1) C_{\rm U}| + |\Psi (y_1 - \Psi x_1) C_{\rm L}|] (1-\Psi^2)^{-1} \\ y_{\max} = [|(y_1 - \Psi x_1) C_{\rm L}| + |\Psi (x_1 - \Psi y_1) C_{\rm U}|] (1-\Psi^2)^{-1}. \end{cases} \tag{3}$$

To increase the uniformity of the spot distribution and to ensure that the pattern area is as large as possible, the rectangle should be close to a square, i.e., $x_{\max}/y_{\max}$ should approximate 1. For a given pattern, the boundary shape is determined by the position of the first spot (x_1, y_1). To quantify the optimum injecting direction, (x_1, y_1) can be rewritten in the polar coordinates as

$$x_1 = r_1 \cos(\Theta), y_1 = r_1 \sin(\Theta), \tag{4}$$

where r_1 is the oscillating magnitude and Θ is the polar angle. r_1 will be divided when calculating for $x_{\max}/y_{\max}$. Therefore, only variations in Θ are considered to affect the $x_{\max}/y_{\max}$ value. For N=87, we calculated all combinations of even $M_{\rm U}$ and $M_{\rm L}$ under $2N$ in the Θ range of 0 to π at a step of 0.01. Each optimum polar angle $\Theta_{\rm opt}$ yielding a $x_{\max}/y_{\max}$ value that most approximates 1 was then recorded. The original and fitted relationships between the twist angle τ and respective $\Theta_{\rm opt}$ of each pattern are shown in Fig. 2. The near-unity value of R^2 indicates that the variability in the data set is well-accounted for by a linear model. The slope of the fitted model is 0.984, indicating that τ can be used as a good approximation of $\Theta_{\rm opt}$ for each pattern. Calculations for other N yield nearly the same results.

After determining Θ by $\Theta_{\rm opt} \approx \tau$, one can scale the pattern size to fill the mirror area better by adjusting the value of r_1. However, this scaling is limited by $r_{\min}$, which is the distance between the nearest spot on M_1 and the origin. If $r_{\min}$ is too small, r_1 should be sufficiently large to prevent the nearest spot from being clipped by the hole edge. As a result, a larger mirror radius is necessary to ensure that the farthest spot remains on the mirror surface. By assuming that the distance between the farthest spot and origin is $r_{\max}$, patterns with the maximum ratio of $r_{\min}$ to $r_{\max}$ are preferred. Figure 3 shows the $r_{\min}/r_{\max}$ values of all patterns for N=501. The pattern locations are plotted as ($M_{\rm U}/2N$, $M_{\rm L}/2N$), and the color indicates the exact $r_{\min}/r_{\max}$ value. The regularity of Fig. 3 is due to the periodicity of the cosine function. Patterns with minimum $r_{\min}/r_{\max}$ are located at the corners of this map and regions where $M_{\rm U,\ L}$ are approximated to N. In Fig. 3, the highest $r_{\min}/r_{\max}$ value is 10 times larger than the smallest one. Therefore, by choosing the "red" patterns, the mirror radius can be 10 times smaller for a similar hole size. Again, calculations for a higher or smaller N give the same results but with different resolutions in the solution space. This conclusion holds true for the subsequent discussions.

When patterns with high $r_{\min}/r_{\max}$ are chosen, the spots on the mirror surface are closely distributed, and some of the spots may overlap. Given the scattering at the mirror's reflective surface, overlapping beam radiation will interfere with the laser beam and may ultimately hit the detector when the radiation travels in the laser beam direction. The recording spectra will then be superimposed by an etalon structure, i.e., the interference fringes noise and the sensitivity will be decreased.

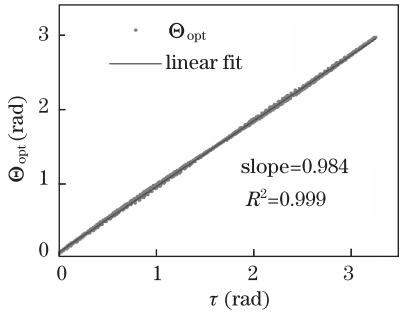

Fig. 2. Linear relationship between the twist angle τ and respective $\Theta_{\rm opt}$ of each pattern.

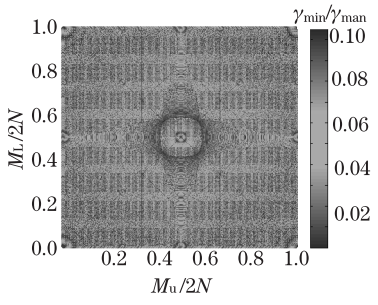

Fig. 3. $r_{\min}/r_{\max}$ values of all patterns for N=501.

The fringes caused by the overlapping between spots with small pass number differences are most problematic because these fringe periods are comparable with the width of the absorption line. The typical pass numbers that must be considered are 4 to 10 passes[10]. We calculated the minimum spot distances $\Delta r_{\min}$ for each pass number difference for all patterns with N=501 according to Eq. (1). The results are shown in Fig. 4. Given the highly similar patterns on M_1 and M_2, only the patterns on M_2 were calculated. The solution space is also based on ($M_{\rm U}/2N$, $M_{\rm L}/2N$). The color indicates the exact value. In Fig. 4, several "zero" bands (dark blue regions) are observed at ξ/Δ, where Δ is the pass number difference and $\xi = 2, 4, \cdots \Delta$. These bands can be explained as follows: from Eq. 1, the spot distances depend on $\sin[(N+\Delta+0.5)\,\theta_{\rm U,\,L}] - \sin[(N+0.5)\,\theta_{\rm U,\,L}]$. Thus, $\Delta r_{\min}$ will be zero when $\theta_{\rm U,\,L} = \xi\pi/\Delta$, i.e., $M_{\rm U,\,L}/2N = \xi/\Delta$. Moreover, when $M_{\rm U}/2N$ equals 1/3 and 2/3, the spot distances are greater than the adjacent patterns for most values of $M_{\rm L}/2N$, as illustrated by the two straight lines in Fig. 4. Note that the patterns at the central part of the solution space have small $\Delta r_{\min}$ for all four pass number differences and may have greater fringe noise. When we consider multiple low-order fringes, zones near odd multiples of $1/\Delta$ are preferred. Pattern stability is another important factor when designing multipass cells, particularly during field measurements. Vibrations, accelerations, ambient temperature and pressure variations, and other changes will lead to variations in mirror distance as well as in rotation angle. In turn, the cell ranges from pattern to pattern, and the performances of spectrometers are reduced[11]. The effects of small deviations Δd or $\Delta\tau$ can be determined using the derivatives of x_{2N} and y_{2N} with respect to d and τ. By taking Δd as an example, the variations in x_{2N} and y_{2N} with d are

$$\Delta x_{2N} = \frac{\partial x_{2N}}{\partial d}\Delta d, \quad \Delta y_{2N} = \frac{\partial y_{2N}}{\partial d}\Delta d. \tag{5}$$

Therefore, the maximum allowed Δd is calculated by

$$(\Delta d)_{\max} = \frac{r_{\rm hole}}{\sqrt{\left(\frac{\partial x_{2N}}{\partial d}\right)^2 + \left(\frac{\partial y_{2N}}{\partial d}\right)^2}}. \tag{6}$$

The relation for calculating $(\Delta\tau)_{\max}$ is analogous. Numerical simulations of all patterns for $(\Delta d)_{\max}$ and $(\Delta\tau)_{\max}$ for N=501 are shown in Figs. 4 and 5, respectively. In a similar manner, the pattern locations plotted as ($M_{\rm U}/2N$, $M_{\rm L}/2N$) and the color (logarithmically) indicates the exact values of $(\Delta d)_{\max}$ and $(\Delta\tau)_{\max}$. In the two simulations, Θ is set to τ, whereas $r_{\rm hole}$, g, and r_1 are all normalized for convenience. Figures 5 and 6 show smoother curves than Fig. 3 because the variations in $(\Delta d)_{\max}$ and $(\Delta\tau)_{\max}$ between adjacent patterns in the solution space are gradient. Patterns with the largest $(\Delta d)_{\max}$ and $(\Delta\tau)_{\max}$ are located at regions where $M_{\rm U,\,L}$ are approximated (not simultaneously) to N. However, according to Fig. 3, the patterns at these regions are distributed relatively uniformly and normally require larger mirror radii. Thus, the choice of pattern is a balance between stability and mirror size. When one specific pattern is chosen, the total path length is the sum of the lengths of all slant rays[12]; i.e.,

$$L = \sum_{n=1}^{2N} L_n = \sum_{n=1}^{2N} \sqrt{d^2 + (x_n - x_{n-1})^2 + (y_n - y_{n-1})^2}, \tag{7}$$

where L_n is the distance between consecutive reflex spots.

The practical design of a cylindrical multipass cell is based on the requirement for monitoring the oxygen concentration in a cabin environment. Thus, the cell should be miniature-sized, stable, and has low fringe noise to ensure sensitivity. Using Figs. 3 to 6 as guides, we found that patterns located at the first quadrant in the ($M_{\rm U}/2N$, $M_{\rm L}/2N$) space are suitable. Indicated as $\{N, M_{\rm U}, M_{\rm L}\}$, the pattern we chose is {87, 44, 50}, which corresponds to dg = 1.1314 and τ=41.03°. This pattern is located at (0.25, 0.29) in the solution space. From Fig. 3, the $r_{\min}/r_{\max}$ of this pattern is 0.16. Therefore, with a hole radius of 2.5 mm, the mirror radius should not be less than 15.6 mm. By considering the practical beam size and the cell volume, we chose cylindrical mirrors with 38-mm radii and 106.9-mm focal lengths. The front mirror has a 5-mm-diameter central hole. Thus, the total volume is 0.55 L, without fittings. Both mirrors are coated with silver (nominal

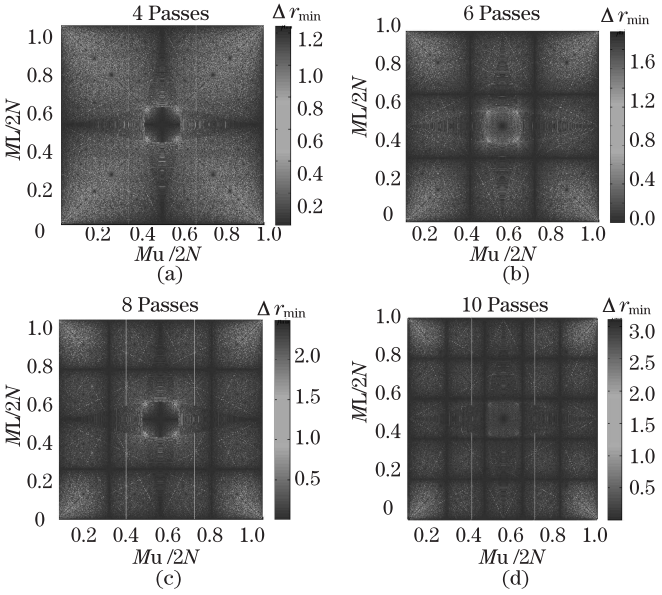

Fig. 4. Minimum spot separations for all patterns with N=501 at a given pass number difference.

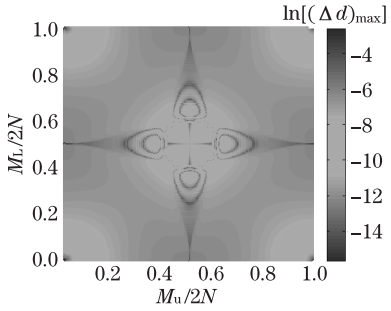

Fig. 5. Maximum allowed variation of d for all patterns with N=501.

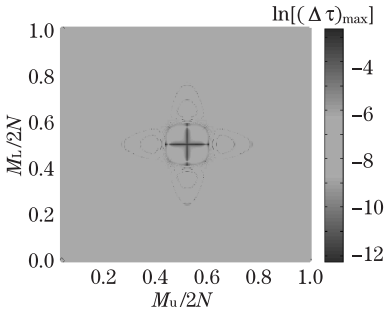

Fig. 6. Maximum allowed variation of τ for all patterns with N=501.

reflectivity is 98%) to reduce reflection loss. Two three-dimensional (3D) aluminum adjusting racks that can provide precise control over translation and rotation are used to the assemble mirrors. The cell is enclosed in a cuboid box constructed with aluminum. Eight blind holes are drilled in two parallel rows into the bottom aluminum board of the box to lock the racks. A broad-band dielectric coated transparent window is inserted into one side board of the box to be used as the coupling window. The front mirror is placed very close to this window, which is deliberately tilted to prevent interference between the incident and reflective beams. The top of the box is made of organic glass, which not only provides clear observation of the spot patterns, but also reduces the overall weight. Two air cocks are mounted on the glass to allow gas exchange. The ultimate dimension of this cell is 25×10×10 (cm), and its weight is only 1.5 kg.

To determine the usefulness of this cell in gas concentration monitoring applications, a simple oxygen sensing experiment that uses tunable diode laser absorption spectroscopy (TDLAS) was performed. The experimental setup is illustrated in Fig. 7. The laser source was VCSEL (Avalon Photonics) and was tuned to emit light around the P9P9 line (13 091.7 cm^{-1}) in the oxygen A band. Transmitted light was transformed to current by a Si photodiode. The amplified electronic signal was acquired by a 16-bit DAQ card. Although the VCSEL output beam is visible, its low power (∼0.6 mW) complicated the direct visualization of the mirror spots. Therefore, a coaligned He–Ne laser was used in the initial alignment. Using a transflective mirror, the He–Ne laser traced the same path as the VCSEL. The position of the first spot on M_2 was controlled by adjusting the flat mirror. In this experiment, the position of the first spot was set to a magnitude of approximately 18 mm and a polar angle of around 41°. The calculated and observed spot patterns on M_1 at this initial beam direction are shown in Fig. 8. The path length was determined as 21.97 m according to Eq. 7. The direct absorption signal of 2.5% standard oxygen under this path length is shown in Fig. 9. The horizontal coordinates were converted from the sample points to the relative wavenumbers by assuming a 0.0491 cm^{-1} half-width at half-maximum according to HITRAN 2008[13]. A Voigt lineshape fit was performed by ORIGIN, and the standard deviation of the residuals was 6.54×10^{-4}. With a peak absorbance of 0.059, a signal-to-noise ratio (SNR) of 90 can be estimated. Thus, the detection limit was determined as 278 ppm. Notably, the unwanted fringes in this pattern are below 6.54×10^{-4}.

With the initial injecting condition of r_1 = 18 mm and a hole radius of 2.5 mm, the maximum allowed variations of d and τ were calculated as 0.095 mm and 0.044°, as shown in Figs. 5 and 6, respectively. Although the mirror twist can be controlled by careful locking, the additional variation in the distance as a result of thermal drift is normally unavoidable. The coefficient of thermal expansion of aluminum is 2.36×10^{-5} K^{-1}. With a base length of 120.9 mm, a 0.095-mm variation in distance corresponds to a temperature change of 33 K. This change is stable enough for the relatively closed cabin environment. By using a larger hole size (on condition that the nearest spot does not exit from the hole) or using low-thermal expansion materials in the construction, the stability of this cell can be improved. In turn, the cell can be used in harsh industrial environments.

In conclusion, an extensive discussion of design considerations for a cylindrical multipass cell is presented. We find the existence of a trade-off between minimizing the mirror sizeminimizing the mirror size and maximizing the pattern stability according to numerical simulation results. A survey of spot spacing properties

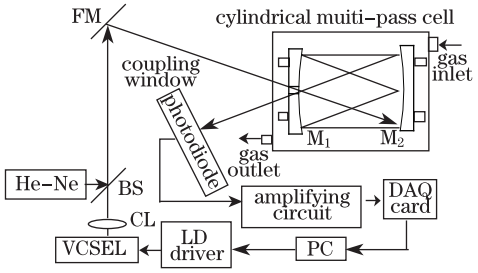

Fig. 7. Diagram of the experimental setup for oxygen sensing. FM: flat mirror; BS: beam splitter; CL: collimating lens.

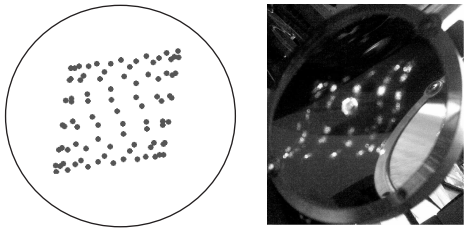

Fig. 8. (a) Calculated spot pattern {87, 44, 50} on M_1. (b) Observed spot pattern {87, 44, 50} on M_1.

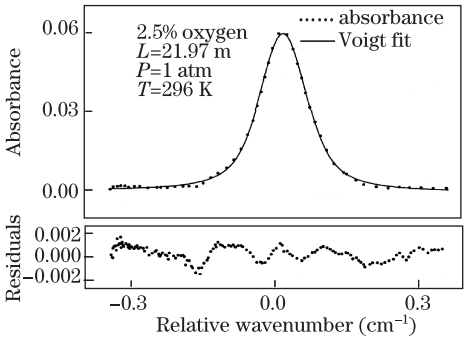

Fig. 9. Direct absorption signal and fitting residuals of 2.5% oxygen at 13 091.7 cm^{-1}.

for all patterns under N=501 shows the locations of patterns with wide spacings at low pass differences. A 0.55-L cylindrical cell with a 121-mm base length has been constructed. By using the {87, 44, 50} pattern and the optimum injecting condition, the total path length is determined as 21.97 m. This pattern remains stable during a temperature change of 33 K. The interference fringes are lower than 6.54×10^{-4} based on an oxygen sensing experiment by TDLAS. The developed cell is suitable for use in compact laser absorption spectrometers for a wide variety of gas-monitoring applications.

This work was supported by the National Key Scientific Instrument and Equipment Development Project under Grant No. 2012YQ22011902.

References

1. L. Wang, Y. Zhang, H. Li, Y. Zhou, K. You, Y. He, and W. Liu, Chin. Opt. Lett. **10,** 350 (2012).
2. Y. Tang, W. Liu, R. Kan, Y. Zhang, D. Chen, S. Zhang, and J. Ruan, Chin. Opt. Lett. **10,** 041404 (2012).
3. J. A. Silver, Appl. Opt. **44,** 6545 (2005).
4. V. L. Kasyutich and P. A. Martin, Appl. Phys. B **88,** 125 (2007).
5. V. L. Kasyutich, Appl. Phys. B **96,** 141 (2009).
6. D. Das and A. C. Wilson, Appl. Phys. B **103,** 749 (2011).
7. A. Khorsandi, Z. Shabani, M. Ranjbar, and S. A. H. Salati, Chin. Phys. B **21,** 213 (2012).
8. A. Manninen, B. Tuzson, H. Looser, Y. Bonetti, and L. Emmenegger, Appl. Phys. B **109,** 461 (2012).
9. J. B. McManus, Appl. Opt. **46,** 472 (2007).
10. J. B. McManus, M. S. Zahniser, and D. D. Nelson, Appl. Opt. **50,** 74 (2011).
11. C. Dyroff, A. Zahn, W. Freude, B. Jänker, and P. Werle, Appl. Opt. **46,** 4000 (2007).
12. J. Altmann, R. Baumgart, and C. Weitkamp, Appl. Opt. **20,** 995 (1981).
13. L. S. Rothman and I. E. Gordon, A. Barbe, D. C. Benner, P. E. Bernath, M. Birk, V. Boudon, L. R. Brown, A. Campargue, J. P. Champion, K. Chance, L. H. Coudert, V. Dana, V. M. Devi, S. Fally, J. M. Flaud, R. R. Gamache, A. Goldman, D. Jacquemart, I. Kleiner, N. Lacome, W. J. Lafferty, J. Y. Mandin, S. T. Massie, S. N. Mikhailenko, C. E. Miller, N. Moazzen-Ahmadi, O. V. Naumenko, A. V. Nikitin, J. Orphal, V. I. Perevalov, A. Perrin, A. Predoi-Cross, C. P. Rinsland, M. Rotger, M. Simeckova, M. A. H. Smith, K. Sung, S. A. Tashkun, J. Tennyson, R. A. Toth, A. C. Vandaele, and J. Vander Auwera, J. Quantum Spectroscopy Radiative Transfer. **110,** 533 (2009).